Atomistic three-dimensional coherent x-ray imaging of nonbiological systems

Phay J. Ho,[1,*] Chris Knight,[2] Miklos Tegze,[3] Gyula Faigel,[3] C. Bostedt,[1,4] and L. Young[1,5]

[1]*Argonne National Laboratory, Argonne, Illinois 60439, USA*
[2]*Leadership Computing Facility, Argonne National Laboratory, Argonne, Illinois 60439, USA*
[3]*Institute for Solid State Physics and Optics, Wigner Research Centre for Physics, Hungarian Academy of Sciences,*
H-1525 Budapest, P.O. Box 49, Hungary
[4]*Department of Physics, Northwestern University, Evanston, Illinois 60208, USA*
[5]*Department of Physics and James Franck Institute, The University of Chicago, Chicago, Illinois 60637, USA*

We computationally study the resolution limits for three-dimensional coherent x-ray diffractive imaging of heavy, nonbiological systems using Ar clusters as a prototype. We treat electronic and nuclear dynamics on an equal footing and remove the frozen-lattice approximation often used in electronic damage studies. We explore the achievable resolution as a function of pulse parameters (fluence level, pulse duration, and photon energy) and particle size. The contribution of combined lattice and electron dynamics is not negligible even for 2 fs pulses, and the Compton scattering is less deleterious than in biological systems for atomic-scale imaging. Although free-electron scattering represents a significant background, we find that recovery of the original structure is in principle possible with 3 Å resolution for particles of 11 nm diameter.

I. INTRODUCTION

X-ray free electron lasers (XFELs) [1–4] have opened a new frontier for x-ray science [5] and an extreme regime for light-matter interactions. Unprecedented focused intensities at ultrashort wavelengths have led to the discovery of x-ray phemonena such as nonlinear multiphoton absorption in atoms, molecules, and clusters [6–10], atomic x-ray lasing [11,12], induced transparency or saturable absorption [6,9,10,13–15], stimulated emission [16–18], and second harmonic generation [19]. Understanding these fundamental processes underpins the use of ultraintense XFEL pulses and fuels the dream of 3D imaging of single biomolecules using the "diffract-before-destroy" method initially envisioned at the dawn of the XFEL-enabled era of x-ray science [20,21].

Research in quest of atomic-scale 3D imaging of isolated biomolecules at XFELs has been extensive, as many functionally interesting systems resist crystallization at a quality sufficient for Å-level diffraction with traditional synchrotron light sources. With XFEL pulses the required size and quality of the crystals has been markedly reduced, sometimes to submicron dimensions [22], structures have been determined to 1.9-Å resolution [23], *de novo* structure determination has been demonstrated [24], and non-Bragg data from imperfect crystals has been used to improve resolution [25]. In this serial femtosecond crystallography [22] method, the concept of self-terminating Bragg gates [26,27] has been essential to extract information from pulses longer than the 10 fs duration estimated to eliminate Coulomb explosion. Importantly, researchers have progressed beyond model systems to deduce structures of biologically interesting entities [28,29].

Not surprisingly, the progress toward noncrystalline single particle 3D imaging has been less rapid [30]. The loss of the N^2 enhancement in coherent elastic scattering inherent to a crystal with N unit cells, magnifies the impact of

photon backgrounds arising from incoherent and free electron scattering and places a stricter requirement on understanding the nature of electronic damage [31–35]. The time scales of electronic rearrangement, Auger decay, nuclear motion, nanoplasma formation, Coulomb explosion, and ion-electron recombination are inconveniently similar and comparable to the femtosecond XFEL pulse duration, placing inherent limitations on the structural precision attainable from coherent diffractive imaging. The dynamics initiated by the imaging pulse have been considered using continuum models [36,37], and with molecular dynamics approaches [21,38,39] which, unlike the continuum approach, hold the promise of atomistic tracking. In an early XFEL experiment, 2D imaging of a mimi virus was demonstrated to 30 nm [40]. Very recently, 3D images using that data set were obtained after orientation and reconstruction [41] of a set of 2D images, at resolution of ∼125 nm [42]. The attained resolution is rather distant from the desired 3 Å, highlighting the importance of understanding fundamental processes of electronic and nuclear dynamics and imaging holistically as recently reviewed [43].

Here we address 3D imaging of nonbiological, high-Z systems at atomic resolution. Understanding 3D imaging in atomic clusters can be considered a first step toward inorganic or metallic clusters such as those that can be formed with atomic-scale precision and are of interest for catalytic, sensing, biological labeling and photonic applications [44–46]. The functionality of nanosystems is governed by their structure and dynamical response, even on ultrafast time scales [47]. By studying heavier systems beyond the second row elements of biological systems, we investigate the changing roles of inelastic vs elastic scattering vs photoabsorption at the extreme intensities and short wavelengths required for imaging, 10^{20} W/cm^2 at 1.5 Å. Simplistically, one expects the inelastic (Compton) scattering to play a reduced role in systems comprised of heavier atoms relative to biological systems, because the ratio of the inelastic to elastic scattering is substantially decreased at wavelengths required for atomic-scale imaging; at 8 keV (1.5 Å) the ratio of the inelastic to elastic cross

063823-1

sections for argon is 0.09 versus 0.6 for carbon. We examine the frozen-nuclei assumption, essentially the Born-Oppenheimer approximation, often used in studies focusing on electronic damage [32,33,35] by simultaneously treating the electron and nuclear dynamics and the coherent diffractive imaging process with a hybrid quantum–classical molecular dynamics approach. Finally, we address the particle size and pulse parameter requirements for 3D imaging as set by the need to classify and orient the coherent diffraction patterns [41,48–53].

We choose as our target nanoscale Ar clusters. Existing XFEL measurements on Ar atoms through Ar_{1000} clusters of ion and electron yields as a function of photon energy, pulse duration, and fluence [10,54] allow us to validate our model and approach to understanding 3D imaging for nanoscale systems. Furthermore, there is intrinsic interest in the study of atomic clusters where the composition and structure can be controlled as a testing ground for new regimes of intense laser-matter interaction [55,56]. Rare gas clusters, bound by easy-to-model van der Waals forces, have traditionally served as testbeds as intense lasers have evolved from optical to x-ray wavelengths [10,38,57–64]. FEL-induced transient dynamics in rare gas clusters have been observed in imaging experiments in the XUV [65] and, more recently, in the x-ray regime [66] providing evidence for femtosecond time scale electronic damage.

This paper is organized as follows. In Sec. II, we describe the hybrid quantum Monte Carlo and classical molecular dynamics method, hereafter referred to as MC-MD. In Sec. III, the impact of ultrafast XFEL multiphoton ionization on the scattering response of nanoclusters and the feasibility of achieving atomic resolution reconstruction with phase retrieval algorithms are discussed. Also, we examine the XFEL wavelength and particle size dependence of the fluence requirements for orientation recovery. Finally, a summary of our results and an outlook is presented in Sec. IV.

II. METHOD

We employ the MC-MD approach to model both the ionization dynamics and scattering response of a nanosized cluster in an intense x-ray pulse. The advantage of this approach is that it can capture the interrelated electron and nuclear dynamics driven by sequential multiphoton absorption in nanometer-sized samples and connect the impact of these dynamics on measured scattering signals. Specifically, the method accounts for initial high-energy photoelectron escape that leads to a charged cluster, which traps low-energy electrons that can, in turn, generate secondary ionization, electron-ion recombination, hydrodynamic motion, and/or Coulomb explosion. All these processes can take place at time scales comparable to the femtosecond x-ray pulse duration. A molecular dynamics (MD) algorithm is used to propagate particle trajectories (atoms or ions or electrons) forward in time and the quantum nature of interactions with an XFEL pulse is treated with a Monte Carlo method [67,68] to determine the time-dependent quantum transition probability between different electronic configurations. The overall transition rate, Γ, between different electronic configurations I and J is given by

$$\Gamma_{I,J} = \Gamma_{I,J}^P + \Gamma_{I,J}^A + \Gamma_{I,J}^F + \Gamma_{I,J}^{EI} + \Gamma_{I,J}^{RC}. \qquad (1)$$

Starting from the ground state of the neutral atom, we include the contribution from photoionization $\Gamma_{I,J}^P$, Auger decay $\Gamma_{I,J}^A$, fluorescence $\Gamma_{I,J}^F$, electron-impact ionization $\Gamma_{I,J}^{EI}$, and recombination $\Gamma_{I,J}^{RC}$. Since the Monte Carlo method is used, 100 replicas of the MC-MD calculations are needed to accurately depict the transient electronic dynamics in Ar clusters presented in this paper. The electronic excitation from Compton scattering is not included as its cross section is 3–4 orders of magnitude smaller than the photoionization process in the considered photon energy range. In addition, the contribution from resonant excitation channels, which are found to be critical in soft x-ray regime for high charge state production [8,67], are not included in our calculations for Ar clusters at 4 and 8 keV. At 8 keV, the single-photon ionization limit is exceeded for all Ar charge states, so the resonant excitation channel is unimportant. At 4 keV where the single-photon ionization limit is 16+, resonant excitation can play a role. While our 4 keV calculations may underestimate the production of highly charged ions, these ions, with $\leqslant 2$ electrons, contribute relatively small scattering signals.

The importance of understanding transient dynamics is that the incoming photons arriving at different times will scatter off the instantaneously populated transient states. The observed scattering response can be characterized as a sum of the instantaneous scattering patterns weighted by the pulse intensity, $j_X(\tau,t)$ with FWHM duration τ. Here we are interested in atomic resolution reconstruction, which requires scattering at high q values. In this case, the scattering signals expressed in terms of the total differential cross section of the cluster can be regarded as the sum of the coherent, free-electron, and Compton (inelastic) scattering [34,69–71]

$$\frac{d\sigma_{\text{total}}}{d\Omega}(\boldsymbol{q}) = \frac{d\sigma_{\text{coh}}}{d\Omega}(\boldsymbol{q}) + \frac{d\sigma_{e^-}}{d\Omega}(\boldsymbol{q}) + \frac{d\sigma_{\text{comp}}}{d\Omega}(\boldsymbol{q}), \qquad (2)$$

where coherent scattering can be expressed as

$$\frac{d\sigma_{\text{coh}}}{d\Omega}(\boldsymbol{q}) = \frac{d\sigma_{th}}{d\Omega} \frac{1}{\mathscr{F}} \int_{-\infty}^{+\infty} dt\, j_X(\tau,t) |F_b(\boldsymbol{q},t)|^2, \qquad (3)$$

with $d\sigma_{th}/d\Omega$ being the Thomson scattering cross section and $\mathscr{F} = \int_{-\infty}^{+\infty} dt\, j_X(\tau,t)$ is the fluence of an XFEL pulse. Here $F_b(\boldsymbol{q},t)$ is the time-dependent form factor of the bound electrons of the target cluster and is given by

$$F_b(\boldsymbol{q},t) = \sum_{j=1}^{N_a} f_j(\boldsymbol{q}, C_j(t)) e^{i\boldsymbol{q} \cdot \boldsymbol{R}_j(t)}, \qquad (4)$$

where N_a is the total number of atoms or ions, and $C_j(t)$ and $f_j(\boldsymbol{q}, C_j(t))$ are the electronic configuration and the atomic form factor of the jth atom or ion, respectively. The momentum transfer vector $\boldsymbol{q} = 4\pi \sin(\theta/2)/\lambda$, where λ is the wavelength of XFEL pulse and θ is the scattering angle defined as the angle between the incoming and scattered XFEL beam. The free-electron contribution is proportional to

$$\frac{d\sigma_{e^-}}{d\Omega}(\boldsymbol{q}) = \frac{d\sigma_{KN}}{d\Omega} \frac{1}{\mathscr{F}} \int_{-\infty}^{+\infty} dt\, j_X(\tau,t) N_e(t), \qquad (5)$$

where $d\sigma_{KN}/d\Omega$ is the Klein-Nishina scattering cross section [72]. For our considered x-ray photon energies, 4 and 8 keV, which are much less than the electron rest mass energy,

$d\sigma_{KN}/d\Omega$ can be approximated by $d\sigma_{th}/d\Omega$. $N_e(t)$ is the number of delocalized electrons within the focal region of the x-ray pulse, their positions are followed in the MD code. For a long pulse (>10 fs), the energetically ejected electrons may escape beyond the focal area and will not contribute to the scattering signals.

The contribution from Compton scattering processes is cast in terms of the inelastic scattering function, $S(\boldsymbol{q},t)$ [69]:

$$\frac{d\sigma_{\text{comp}}}{d\Omega}(\boldsymbol{q}) = \frac{d\sigma_{KN}}{d\Omega}\frac{1}{\mathscr{F}}\int_{-\infty}^{+\infty} dt\, j_X(\tau,t)S(\boldsymbol{q},t), \qquad (6)$$

with

$$S(\boldsymbol{q},t) = \sum_{j=1}^{N_a} s_j(\boldsymbol{q},C_j(t)), \qquad (7)$$

and $s_j(\boldsymbol{q},C_j(t))$ is the inelastic scattering function of the jth atom or ion with electronic configuration $C_j(t)$.

The inability to distinguish experimentally the scattering contributions in Eq. (2) means that the scattering from intense XFEL pulses differs from the coherent scattering in the weak-field limit which represents an undamaged sample and is given by

$$\frac{d\sigma_0}{d\Omega}(\boldsymbol{q}) \approx \frac{d\sigma_{th}}{d\Omega}|F_b(\boldsymbol{q})|^2. \qquad (8)$$

The 3D electron $\rho_c(\boldsymbol{r})$ density of the undamaged cluster is then obtained after phase recovery:

$$\rho_c(\boldsymbol{r}) = \int d\boldsymbol{r}\, F_b(\boldsymbol{q})e^{i\boldsymbol{q}\cdot\boldsymbol{r}}. \qquad (9)$$

In this work we investigate the relative importance of bound, free electron, and Compton scattering as a function of pulse parameters, system size, and the degree of deviation from the weak-field limit.

To connect the scattering measurement with the ionization dynamics, we also compute the pulse weighted charge state $(\overline{Q_w})$ and displacement $(\overline{D_w})$ of the atoms and ions, where

$$\overline{Q_w} = \int dt\, j_X(\tau,t)\overline{Q(t)}/\mathscr{F} \qquad (10)$$

and

$$\overline{D_w} = \int dt\, j_X(\tau,t)\overline{D(t)}/\mathscr{F}. \qquad (11)$$

Here, $\overline{Q(t)}$ is the average charge of all atoms and ions at time t and

$$\overline{D(t)} = \sum_{j=0}^{N_a} |\text{R}_j(t) - \text{R}_{j,o}|/N_a \qquad (12)$$

is the average atomic displacement with $\text{R}_j(t)$ and $\text{R}_{j,o}$ being the positions of jth atom at time t and prior to the XFEL pulse, respectively.

A similar methodology was successfully used to model the interactions of C_{60} [73] and 1000-atom Ar clusters [54] exposed to intense XFEL pulses. In the earlier work on C_{60} [73], a systematic study of the effects of molecular bonds, secondary ionization, bond breaking, and molecular Auger for multiple conditions of low, medium, and high fluence. A

bondless approach was found to be sufficient to model C_{60} in the high-fluence, short-pulse conditions that are used for x-ray imaging, whereas for medium fluences it is straightforward to add force fields to account for molecular bonding. More recently, this methodology was used to describe a nitrogenase iron protein in 5 keV x-ray pulses of 9 and 30 fs duration [74], where the addition of Compton scattering was found to deteriorate the achievable resolution. The present study extends the methodology to heavier and larger systems to examine higher-Z effects, but retains the van der Waals interactions. For high-Z systems, the added complexity stems from the need to track a larger number of electronic configurations and transition channels, i.e., several orders of magnitude more than required for organic molecules. None of these atomistic MD methods [54,73,74] yet includes the plasma-induced effect of ionization potential depression (IPD) [75], but we note that the magnitude of the changes in ionization potential (~ 100 eV) contributes only modest changes to photoionization rates and cross sections for hard x-ray energies well above the ionization potentials of the atoms in the system. Including these effects is a topic for future work, as a previous calculation of IPD [76] employs assumptions of fixed nuclei and thermalized electron distributions, neither of which is valid for our finite nanosystem that is rapidly undergoing electron rearrangement and Coulomb explosion. We note that our MC-MD code was validated by reproducing the experimental kinetic-energy distribution of ionized electrons from 1000-atom Ar clusters exposed to intense 5 keV XFEL pulses [54,77].

III. RESULTS

Building on the success of the MC-MD method in describing the experimental spectroscopic observables of Ar cluster in intense XFEL pulses, we further examine the scattering response of these clusters. We will focus on the response over an interesting range of fluences, x-ray photon energies, and particle sizes identified in the single particle imaging initiative [30].

A. Limitations of the frozen lattice approximation

Our ability to include both electronic and ion dynamics on an equal footing allows us to test the validity of the frozen-lattice approximation over a range of pulse parameters. The frozen-lattice approximation has been used in earlier work on electronic damage on biological systems [32,33,35] with the assumption that x-ray pulses of 5 fs are sufficient to freeze the ion motion. In a biological system, the initiating femtosecond dynamics are dominated by the Auger lifetimes of C, N, and O, which are, respectively, 10.7 fs, 7.1 fs, and 4.9 fs, followed by nanoplasma formation and Coulomb explosion. We note that the 1s inner-shell hole lifetime for an argon atom is substantially shorter, ~ 1 fs, and the time scales needed to "freeze" the lattice motion in a heavier system are expected to be correspondingly shorter.

Figure 1 shows the time evolution of a seven-shell Ar cluster (1415 nuclei and 25470 electrons, 5.26 nm diameter) subjected to 8 keV XFEL pulses of 30 fs and 2 fs duration for a fluence of 10^{14} photons/μm^2. In the 30 fs pulse, the atoms or ions are clearly not stationary. Here sequential multiphoton ionization, enhanced by repopulation of inner
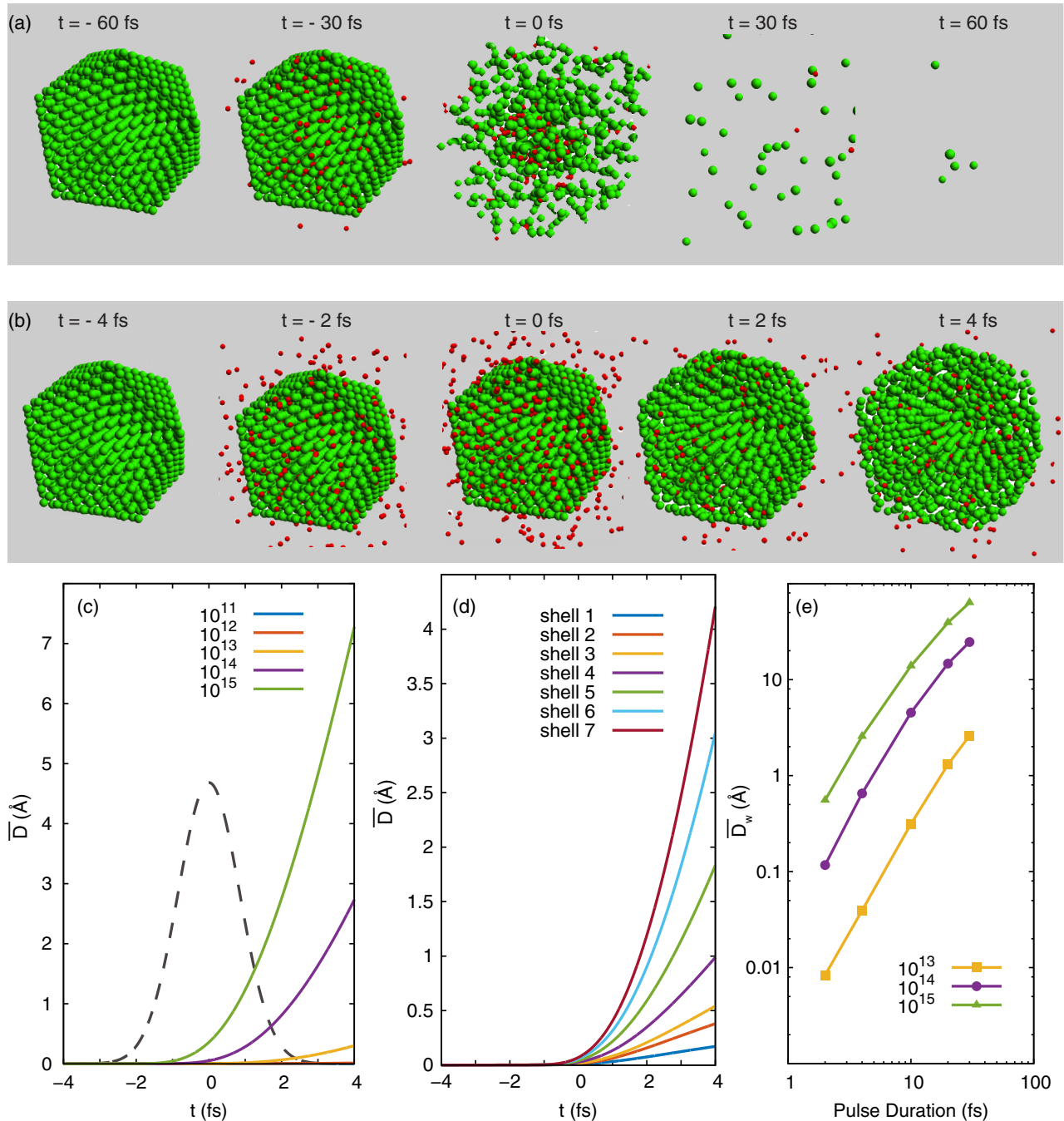
FIG. 1. Snapshots of ionization dynamics of a seven-shell Ar cluster (1415 atoms) induced by an 8 keV, 10^{14} photons/μm^2 pulse with durations (a) 30 fs and (b) 2 fs. The larger green and smaller red particles represent argon atoms or ions and electrons, respectively. (c) Average atom or ion displacement, $\overline{D(t)}$, during a 2 fs pulse as for fluences in the range of 10^{11} (lowermost line) to 10^{15} photons/μm^2 (uppermost line). Fluences lower than 10^{13} photons/μm^2 yielded negligible $\overline{D(t)}$. (d) Average displacement, $\overline{D(t)}$, for atoms originating from seven different geometric shells in the cluster during a 2 fs, 10^{14} photons/μm^2 pulse. The seven lines show the outermost shell (uppermost line) to the innermost shell (lowermost line). (d) Pulse-weighted average displacement, $\overline{D_w}$, as a function of pulse duration and for fluences of 10^{13} (squares), 10^{14} (circles), and 10^{15} photons/μm^2 (triangles).

shells by Auger decay, leads to strong spatial distortion of the electronic distribution and generates a large number of delocalized electrons. The subsequent buildup of Coulombic forces causes disintegration already by the peak of the pulse. In contrast, for the 2 fs pulse the lattice structure remains mostly intact during the rise of the pulse. After the peak of the pulse the cluster shows considerable expansion by 4 fs

where the average displacement of the constituent atoms or ions is 2.8 Å, compared to the internuclear separation of 3.76 Å. In particular, the atoms in the outer shell expand faster than those deep inside the cluster [Fig. 1(d)]. For our nanoscale cluster surface ablation is unavoidable and has been recognized as a challenge for the "diffract-before-destroy" method [78]. Advantageously, for imaging applications only
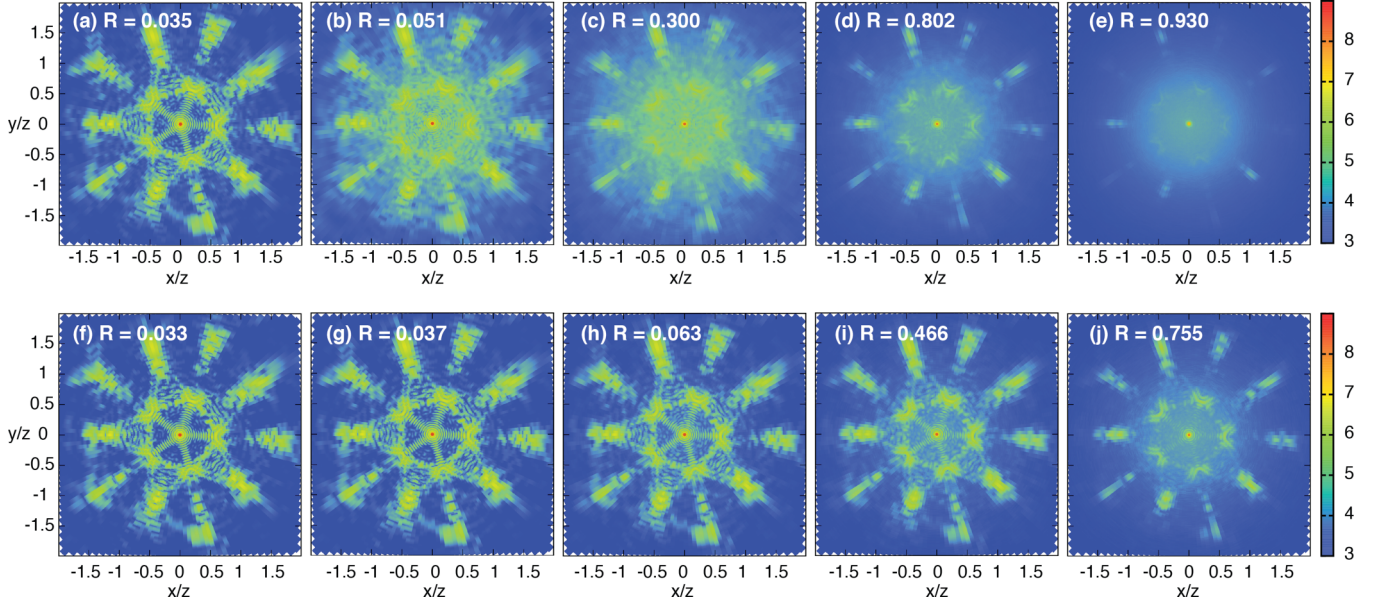
FIG. 2. X-ray diffraction patterns of Ar_{1415} obtained from an 8 keV pulse with 30 fs (top row) and 2 fs (bottom row) duration for five different fluences: 10^{11} (leftmost column), 10^{12}, 10^{13}, 10^{14}, and 10^{15} photons/μm^2 (rightmost column). The color scale is logarithmic, showing the cross section in units of the classical radius of the electron squared, r_e^2. The plots display differential cross sections, rather than photon number, as this representation better reveals the degree of deviation from the undamaged structure.

the displacement present during the x-ray pulse is observed. The pulse-weighted average displacement, $\overline{D_w}$, for the 2 fs, 10^{14} photons/μm^2 pulse is 0.22 Å, which can be compared to vibrational smearing of 0.01 Å at 10 K. Here we note that the fluence of 10^{14} photons/μm^2 is sufficient for atomistic reconstruction, as described in the next section. While previous work assumed validity of the frozen-lattice approximation for the pulse durations <5 fs, we find for a 4 fs (FWHM) pulse substantial expansion for the Ar cluster with a $\overline{D_w}$ of ∼1 Å.

The scattering response also shows the necessity of the shorter pulse duration. The response is governed by the profile of ionization dynamics and consists of three components: coherent scattering from bound electrons, scattering from free electrons, and inelastic (Compton) scattering. Figure 2 shows the scattering response of the seven-shell cluster for x-ray fluence in the range of 10^{11} to 10^{15} photons/μm^2 and pulse durations (FWHM) of 30 fs and 2 fs. In the case of a 30 fs, 10^{11} photons/μm^2 pulse, the interference fringes due to the lattice at small angles and Bragg peaks at large angles are clearly visible. This corresponds to a relatively undamaged sample with a pulse weighted charge state of $\overline{Q_w} = 0.07$, where essentially all of the 18 electrons for each Ar atom remain with their original nucleus enabling coherent atomic scattering. The fluence dependence for $\overline{Q_w}$ is shown in Table I. At higher fluence, the XFEL-induced lattice and electron dynamics on the cluster produces notable changes on the patterns; the interference fringes are distorted, the free-electron contribution to the background becomes clear, and the visibility of the Bragg peaks is reduced, eventually disappearing at $\mathscr{F} = 10^{15}$ photons/μm^2. The 2 fs pulse, by contrast, preserves interference fringes even at $\mathscr{F} = 10^{14}$ photons/μm^2 by limiting the observed lattice motion during the pulse. Thus, as one moves to heavier systems with shorter intrinsic time scales, shorter pulses are required to invoke the frozen-lattice approximation with confidence.

B. Atomistic reconstruction in the face of electronic damage

The recorded scattering patterns at high fluence deviate strongly from the pattern of the undamaged particle. The degree of deviation can be quantified in terms of an R factor [21],

$$R = \frac{\sum_q \left| \frac{d\sigma_{\text{total}}}{d\Omega}(\boldsymbol{q}) - \frac{d\sigma_0}{d\Omega}(\boldsymbol{q}) \right|}{\sum_q \frac{d\sigma_0}{d\Omega}(\boldsymbol{q})}. \tag{13}$$

For the patterns shown in Fig. 2, R ranges from 0.03 to 0.930 for the 30 fs pulse and from 0.03 to 0.755 for the 2 fs pulse. Higher fluence and longer pulse duration yield larger deviations.

An interesting question is the degree of deviation that can be tolerated for a successful high spatial resolution 3D reconstruction. Previous studies use $R < 0.2$ as a guide for enabling reconstruction [21,32] and determining useful XFEL

TABLE I. Pulse weighted average charge state ($\overline{Q_w}$) and the average charge state ($\overline{Q}$) for a seven-shell Ar cluster exposed to 2 fs and 30 fs pulses at 8 keV as a function of fluence. $\overline{Q_w}$ is the average charge state relevant for imaging, whereas $\overline{Q}$ is a measure of the integral charge state resulting from the pulse. $\overline{Q}$ for $\tau = 2$ fs and 30 fs are the values at $t = 3\tau$.

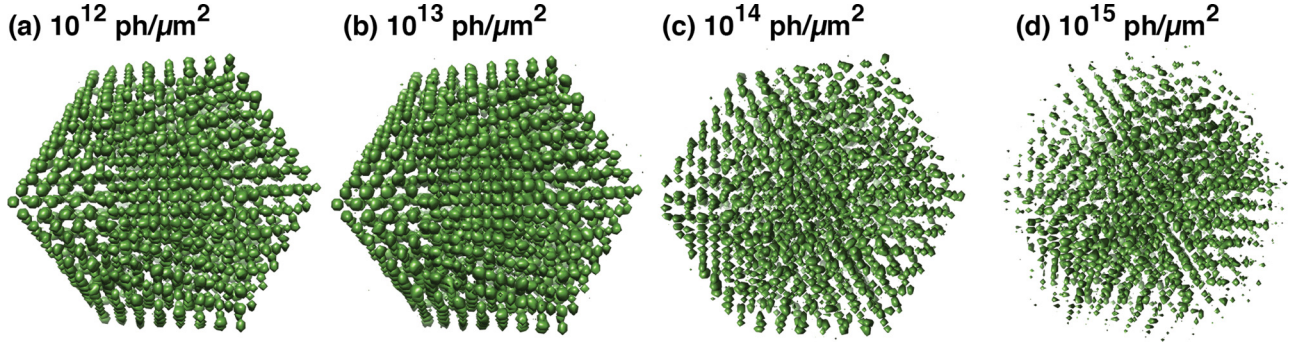| $\mathscr{F}$ (ph/μm^2)	$\tau = 2$ fs		$\tau = 30$ fs	
	$\overline{Q_w}$	$\overline{Q}$	$\overline{Q_w}$	$\overline{Q}$
10^{11}	0.03	0.14	0.07	0.15
10^{12}	0.25	0.78	0.48	0.94
10^{13}	1.77	3.83	2.95	5.88
10^{14}	6.42	10.34	12.72	17.35
10^{15}	11.57	14.93	16.89	17.92

FIG. 3. Reconstructed electron densities (green regions) from the 8 keV, 2 fs scattering patterns with different fluence levels (10^{12} to 10^{15} photons/μm^2).

pulse parameters. This is also the value of R that is typical for deposits in the protein data bank. Here, somewhat surprisingly, we find that we can successfully recover atomistically resolved structure even with an R factor as high as 0.466, as obtained for a 2 fs pulse with a fluence level of 10^{14} photons/μm^2. A detailed comparison of the reconstructed electron density for various pulse parameters is in Appendix A. The individual structures shown in Fig. 3 are obtained by performing a phase retrieval analysis on the 3D diffraction signals calculated for a q-space grid of $101 \times 101 \times 101$ points. In each dimension, the signals are sampled with an interval of $dq = 0.065$ Å^{-1} to reach a maximum amplitude of $q_{max} = 3.24$ Å^{-1} and a spatial resolution of $d = 2\pi/q_{max} = 1.94$ Å, which is smaller than the cluster interatomic spacing of 3.76 Å. The results shown in Fig. 3 are based on the RAAR method [79], but we obtained similar structures also with the HIO method [80]. We point out that successful reconstruction is also achieved on an Ar cluster with an amorphous distribution of initial atomic positions at a fluence level of 10^{14} photons/μm^2, suggesting that the ability to reconstruct is rather insensitive to the initial cluster atomic configuration (see Appendix B).

The original structure is not recovered for $\mathscr{F} = 10^{15}$ at 2 fs and $\mathscr{F} = 10^{14}$–10^{15} photons/μm^2 at 30 fs. For these pulses, the reconstruction does not preserve the outer shell of atoms. These failures stem from the ionization dynamics which produce large values of the pulse-weighted average displacement, $\overline{D_w}$ (>1 Bohr radius), and charge, $\overline{Q_w}$. The 8-keV, 30-fs pulses can fully strip an Ar atom via sequential multiphoton ionization, produce $\overline{Q_w} > 10$, where the scatter-

ing is dominated by free-electron scattering. In comparison, the 2 fs, 10^{14} photons/μm^2 pulse, which enables successful reconstruction, has $\overline{Q} > 10$, but $\overline{Q_w} = 6.42$, implying that the scattering events are primarily from electrons bound to atoms or ions.

C. Compton scattering effects

Previous calculations on intense x-ray scattering from biomolecules consisting of mostly light elements (H, C, N, and O) demonstrate that the presence of Compton (inelastic) scattering can severely compromise the imaging resolution [34,35,74]. Specifically, the contribution to the number of scattered photons per Shannon pixel at high q corresponding to a resolution of 1.5 Å is largely from Compton scattering [34]. Here we investigate the relative contribution of coherent scattering, Compton scattering, and free-electron scattering to the total scattering signals in a heavier system. The number of scattered photons per Shannon pixel is given by

$$N_s(\theta) = \frac{1}{2\pi}\left\langle\frac{d\sigma_{total}}{d\Omega}\right\rangle_\phi \mathscr{F}\Omega_s, \tag{14}$$

where $\frac{1}{2\pi}\langle\frac{d\sigma_{total}}{d\Omega}\rangle_\phi$ is the azimuthally averaged differential cross section and $\Omega_s = \lambda^2/4w^2$ is the size of the Shannon pixel for an object of width w exposed to an incident x-ray field of wavelength λ [41].

Figure 4(a) shows the contribution of coherent, free-electron, and Compton scattering on the scattering signals, $N_s(\theta)$, for an Ar$_{1415}$ cluster in a 8 keV, 2 fs, 10^{14} photons/μm^2
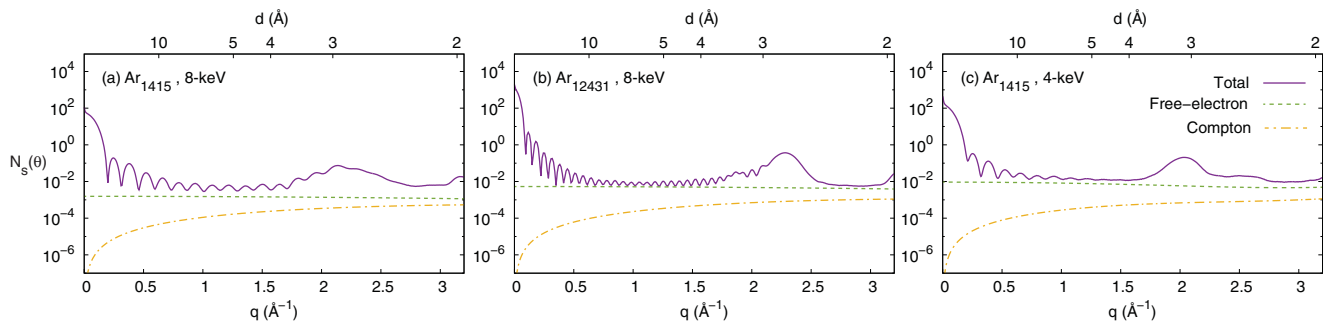

FIG. 4. Total scattering (coherent+incoherent+free electron, purple solid lines), free-electron scattering (green dotted lines), and Compton scattering (orange dashed-dotted lines) for (a) Ar$_{1415}$ in an 8 keV pulse, (b) Ar$_{12431}$ in an 8 keV pulse, and (c) Ar$_{1415}$ in a 4 keV pulse. For all cases, the pulse fluence is 10^{14} ph/μm^2 and duration is 2 fs.

pulse. The angular distribution of free-electron scattering follows the Thomson differential cross section, dropping $\sim$40% from $\theta = 0$ to 60° ($q = 0$ to 3.2 Å^{-1}), while the Compton scattering rises rapidly with θ. The coherent scattering from the bound electrons display maxima arising from the distribution of atoms within the cluster. Unlike the biomolecules, the free-electron scattering in the Ar cluster dominates the Compton scattering even at the high scattering angles corresponding to 3 Å resolution. To compare the Compton effect in Ar clusters with light-element systems, we repeated the calculation replacing the Ar atoms with C atoms on the lattice. We find that the Compton signals from the C cluster overtake the free-electron signals at $q = 0.32$ Å^{-1} and are larger than the coherent signals $q = 0.95$ Å^{-1} for the same pulse parameters. This confirms that in heavier systems the free-electron scattering is more important than the Compton for high-q scattering at imaging intensities.

We further examine Compton scattering as a function of particle size and wavelength. For a larger cluster Ar$_{12431}$ (223758 electrons), Fig. 4(b) shows that the relative contribution from Compton scattering is smaller. With a longer wavelength pulse, which is more efficient in ionization, the contribution from Compton is even smaller and free-electron contribution is more dominant, as shown in Fig. 4(c).

D. Requirements for orientation: Wavelength and size dependence

So far, our discussion has been based on the assumption that 3D diffraction signals can be retrieved from a set of 2D patterns corresponding to different, but known orientations. Advanced algorithms [51–53] allow one to orient patterns at

spatial resolution of d, with diffracted intensities as low as $\sim$0.1 scattered photons per Shannon pixel (N_s) for scattering angles out to $q_{max} = 2\pi/d$, as given by $\sin(\theta/2) = (\lambda/2d)$. Using this criterion, we see that it is possible to orient an Ar$_{1415}$ particle using an extremely high-fluence 8 keV, 2 fs, $10^{15}/\mu$m^2 pulse [Fig. 5(a)]. One can manipulate N_s by exploring different pulse parameters, $\mathscr{F}$ and λ, and particle size, w, as shown in Eq. (14) and discussed below.

We first examine the effects of pulse fluence on Ar$_{1415}$. At 10^{15} μm^2 the reconstructed structure differs significantly from the undamaged Ar$_{1415}$ structure [Fig. 3(d)]. Careful examination of the scattering signal shows that the location of the first minimum is shifted to a larger q, from 0.19 to 0.20 Å^{-1} (a 4% shift in q), for 10^{15} μm^2 compared to the low fluence result. This shift corresponds to the shrinking of the cluster resulting from the escape of delocalized electrons and ablation of atoms from the outer layers. In our calculations, the probability of photoabsorption is a function of $C_j(t)$ and independent of atom location (inner vs surface) within the nanosized cluster. Thus our atomistic model reproduces the different ionization profiles within the cluster (surface ablation dynamics vs mostly static inner atoms) that is a general feature of photon-induced plasma dynamics in finite-sized systems. We note that the ablation process is the major factor for the substantial reduction in scattering cross section at high fluence levels as shown in Fig. 5(e).

We next examine the effects of longer wavelength, 4 keV versus 8 keV, and the changing contributions of the coherent and Compton scattering, and photoabsorption. With respect to the orientation problem, the obvious advantages of a 4 keV photon energy are the larger coherent scattering cross section
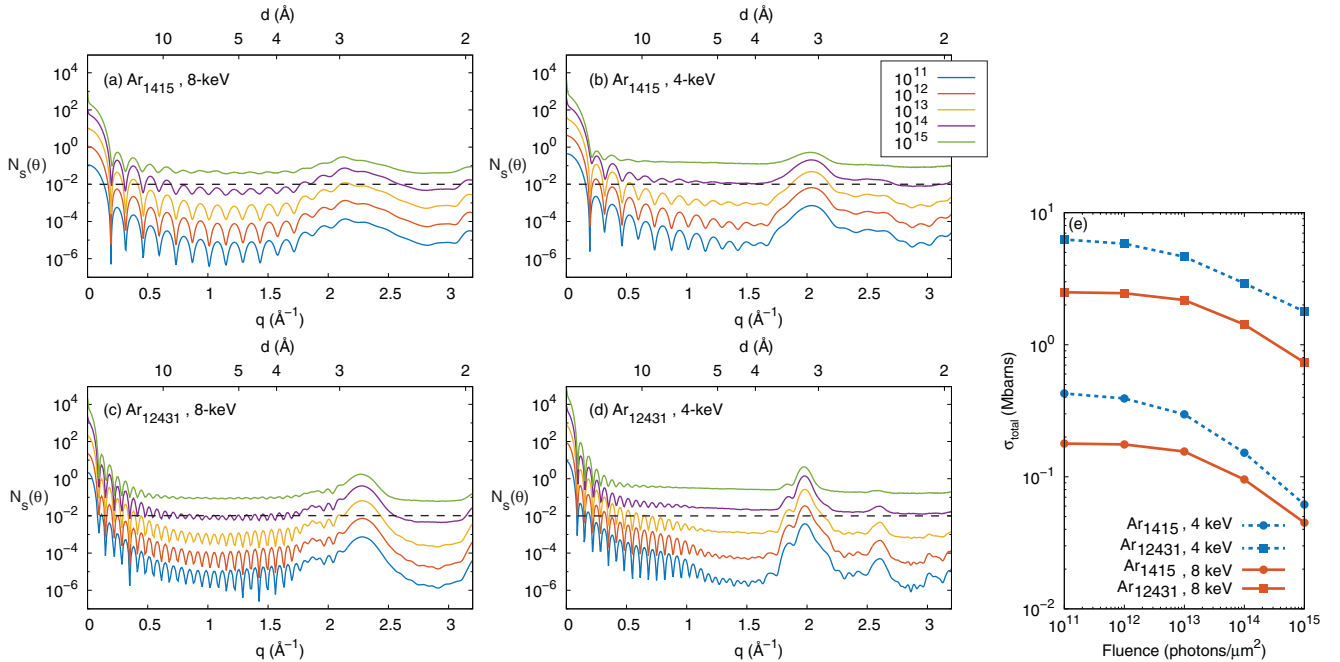

FIG. 5. Number of scattered photons per Shannon pixel, N_s, as a function of q, momentum transfer, and d, desired spatial resolution for a single cluster orientation. Ar$_{1415}$ at (a) 8 keV, (b) 4 keV and Ar$_{12431}$ at (c) 8 keV, (d) 4 keV. All the plots are obtained with a 2 fs pulse; the dashed line indicates $N_s = 0.01$. In each plot, N_s for five different fluences from 10^{11} (lowermost line) to 10^{15} photons/μm^2 (uppermost line) are shown. (e) Total scattering cross sections of Ar$_{1415}$ (circles) and Ar$_{12431}$ (squares) as a function of fluence for 4 keV (dashed lines) and 8 keV (solid lines) photon energy and 2 fs pulse duration. Orientationally averaged scattering is shown in Appendix C.

(a gain of $\sim$1.4 for Ar_{1415} at low pulse fluence), and the larger size of the Shannon pixel $\propto \lambda^2$ (gain of $4\times$). An experimental disadvantage of using a 4 keV pulse is that the signal needs to be collected over a larger range of scattering angles for 3 Å resolution, from 0–61° at 4 keV compared to 0–29° at 8 keV. $N_s > 0.01$ is easily achievable for Ar_{1415} in a 4 keV, 10^{15} μm^2 pulse [Fig. 5(b)] and borderline for 10^{14} μm^2, suggesting that orientation recovery is feasible. However, as pointed out earlier, a higher N_s value does not guarantee a faithful 3D atomistic reconstruction. The overriding disadvantage of a 4 keV pulse is the higher photoabsorption cross section (112 barns/atom at 4 keV vs 61 barns/atom at 8 keV) and associated damage. Both $\overline{D_w}$ and $\overline{Q_w}$ are higher in 4 keV pulse, with $\overline{D_w}$ approaching 1 Å at 10^{15} μm^2. In comparison to the pattern at 10^{11} μm^2, the location of the first minimum in the scattering pattern has a 4% shift in q value already at 10^{14} μm^2. Substantial shape changes resulting from ionization and surface ablation begin at a lower fluence in a 4 keV pulse and prevents recovery of the undamaged Ar_{1415} structure.

Finally, we consider a larger cluster to mitigate the impact of electronic damage, analogous to the use of larger crystals in crystallography, Figures 5(c) and 5(d). For a larger cluster, Ar_{12431} (223758 electrons, 11.3 nm diameter), orientation is clearly feasible at a fluence of 10^{14} μm^2. $\overline{D_w}$ is significantly decreased relative to Ar_{1415}, i.e., by a factor of $\sim$2 to a value of <0.5 Å at the highest fluence. The first minimum in the scattering pattern shifts $<1\%$ in q from the low-fluence value. In addition, the larger cluster has a coherent scattering cross section that scales more rapidly than the simple N_a which represents scattering from independent atoms. Coherent scattering is increased above the independent atom values by factors of 4.5 and 3.2, at 4 and 8 keV, respectively for the larger cluster, versus 2.7 and 2.0 for the smaller cluster, Ar_{1415}, in the low fluence limit. The scaling is slightly less than the size of the particle, w. As the fluence is increased to the levels required for orientation the advantages of the larger cluster are clearly evident in Fig. 5(e), where the upper two curves represent the larger cluster and the lower two the smaller cluster. The total scattering from both clusters decreases as a function of fluence, but the damaging effects of increased fluence are significantly greater in the smaller cluster.

IV. SUMMARY AND OUTLOOK

In summary, we analyzed the ionization dynamics and the corresponding scattering signals for Ar clusters exposed to ultraintense x-ray radiation using our MC-MD method with the aim of exploring atomic-resolution x-ray imaging in heavier, nonbiological systems. We found that, for heavier systems, one needs pulses shorter than the oft-used 5 fs guideline for the frozen-lattice approximation to be valid. We also found that Compton scattering, which plays a deleterious role in light biological systems, is much less of a factor for heavier systems. With respect to the scattering strength needed for atomic-resolution reconstruction of undamaged structures, there is a strong dependence on pulse parameters and advantages to larger systems, because (a) the scattering cross section scales more rapidly than N_A, the independent atom approximation, and (b) the damage is distributed,

similar to the concept of self-terminating diffraction gates in femtosecond nanocrystallography.

For heavier systems like platinum clusters, 3D atomistic coherent diffractive x-ray imaging is expected to be more tractable than for argon. The background from Compton scattering is smaller, with $\sigma_{comp}/\sigma_{coh}$ being $\sim$1% at 8 and 4 keV compared to 10% for argon. Platinum atoms have a more favorable ratio of coherent scattering to absorption at 8 and 4 keV with $\sigma_{coh}(Pt)/\sigma_{coh}(Ar) = 30$ and $\sigma_{abs}(Pt)/\sigma_{abs}(Ar) = 8$. To find the optimal pulse parameters and size in heavy systems like Pt clusters, investigations with MC-MD calculations are needed. The degree of complexity of Pt calculations, however, increases enormously due to the large number of electrons. As a result, a calculation with about 10^4 Pt atoms will entail tracking nearly 1 million particles (electrons + nuclei). A more challenging issue lies in participation of a larger number of electronic transitions in the transient dynamics. In the sequential, multiphoton picture, the number of accessible electronic configurations (ECs) for platinum is $>3 \times 10^8$ at 8 keV where the sequential single photon ionization limit is 68+. By comparison, the number of electronic configurations in Ar is 1323. The 10^5 increase in EC number means that many replicas of MC-MD calculations are needed to converge ionization and scattering profiles. In the case of a 4 keV pulse, hidden resonances [16,67,68], easily accessible at high fluence, become important for the production of ions above 20+. This added complexity will further increase the number of replicas required to account for the many orders-of-magnitude increase in ECs. As a result, high performance computing resources are needed to investigate the ionization dynamics and scattering response of Pt clusters. Our code is highly parallelized and has achieved a good scalability on the high-performance computing platforms with hundred thousands of cores, like Mira, the petaflop-scale computer at Argonne Leadership Computing Facility. The algorithm and codes associated with implementation in a high-performance computing environment will be discussed in a forthcoming paper [77].

APPENDIX A: RECONSTRUCTED ELECTRON DENSITY OF SEVEN-SHELL Ar CLUSTER

We solved the phase problem using the Relaxed Averaged Alternating Reflections (RAAR) algorithm [79] with parameter $\beta = 0.87$ to reconstruct the electron density in real space. Initially, a fixed spherical support with 50 a.u. diameter (slightly larger than the cluster) was used. After 200 iterations convergence was reached. Then we increased
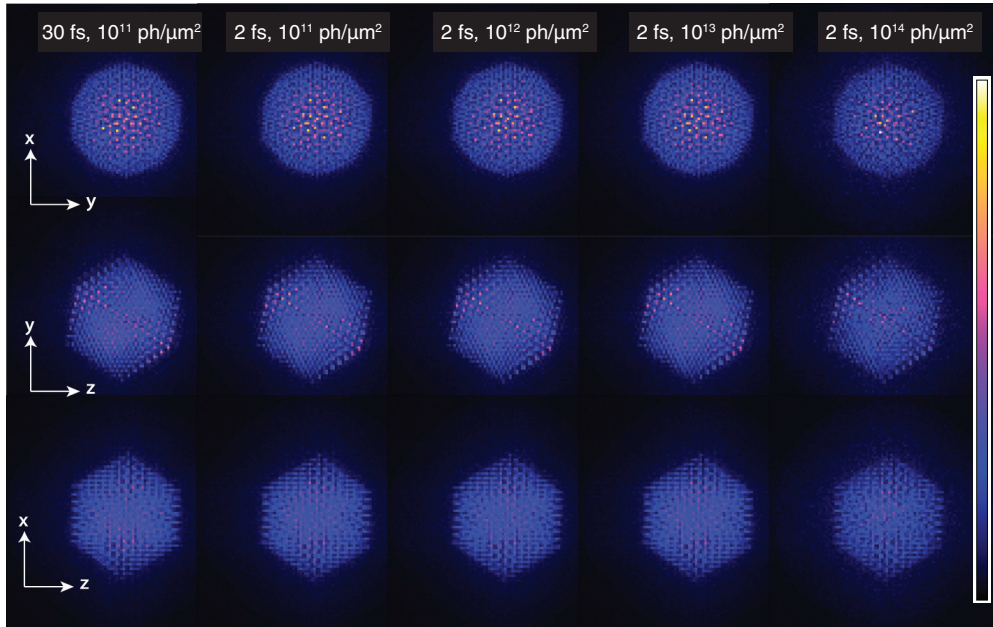
FIG. 6. Reconstructed electron density projected on x-y, x-z, and y-z plane from the scattering pattern calculated at (a) 30 fs, 10^{11} photons/μm^2, (b) 2 fs, 10^{11} photons/μm^2, (c) 2 fs, 10^{12} photons/μm^2, (d) 2 fs, 10^{13} photons/μm^2, and (e) 2 fs, 10^{14} photons/μm^2 using the RAAR algorithm.

the support diameter to 90 a.u. to avoid truncation of the outer regions of electron density and performed 100 more RAAR iterations. Last, we applied 100 iterations of the Error Reduction (ER) [80] algorithm to reconstruct the final electron density. Figure 6 shows that reconstructed electron density with the RAAR projected on x-y, x-z, and y-z plane for different pulse parameters.

Scattering of photons on ions and electrons were calculated according to Eqs. (2)–(7) of the main paper. Since detailed testing of the orientation process was not the subject of our study, 2D scattering patterns with many random orientations of the cluster were not produced. The 3D scattering patterns were calculated on a q-space grid of $101 \times 101 \times 101$ points with time steps of 0.001 fs for both the 2 fs and 30 fs pulses. The resulting scattering intensities (cross sections weighted
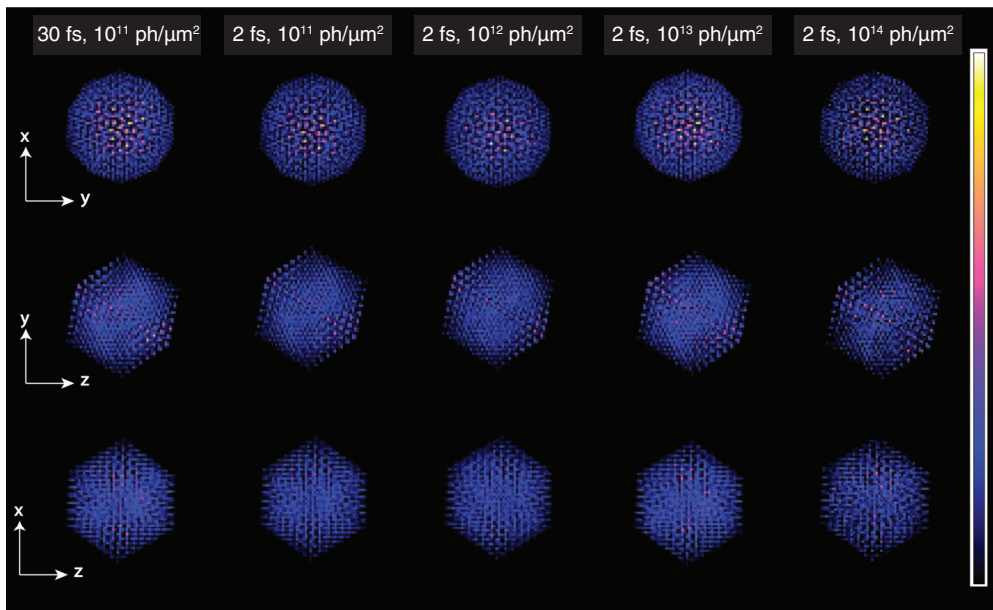

FIG. 7. Reconstructed electron density projected on x-y, x-z, and y-z plane from the scattering pattern calculated at (a) 30 fs, 10^{11} photons/μm^2, (b) 2 fs, 10^{11} photons/μm^2, (c) 2 fs, 10^{12} photons/μm^2, (d) 2 fs, 10^{13} photons/μm^2, and (e) 2 fs, 10^{14} photons/μm^2 using HIO algorithm.
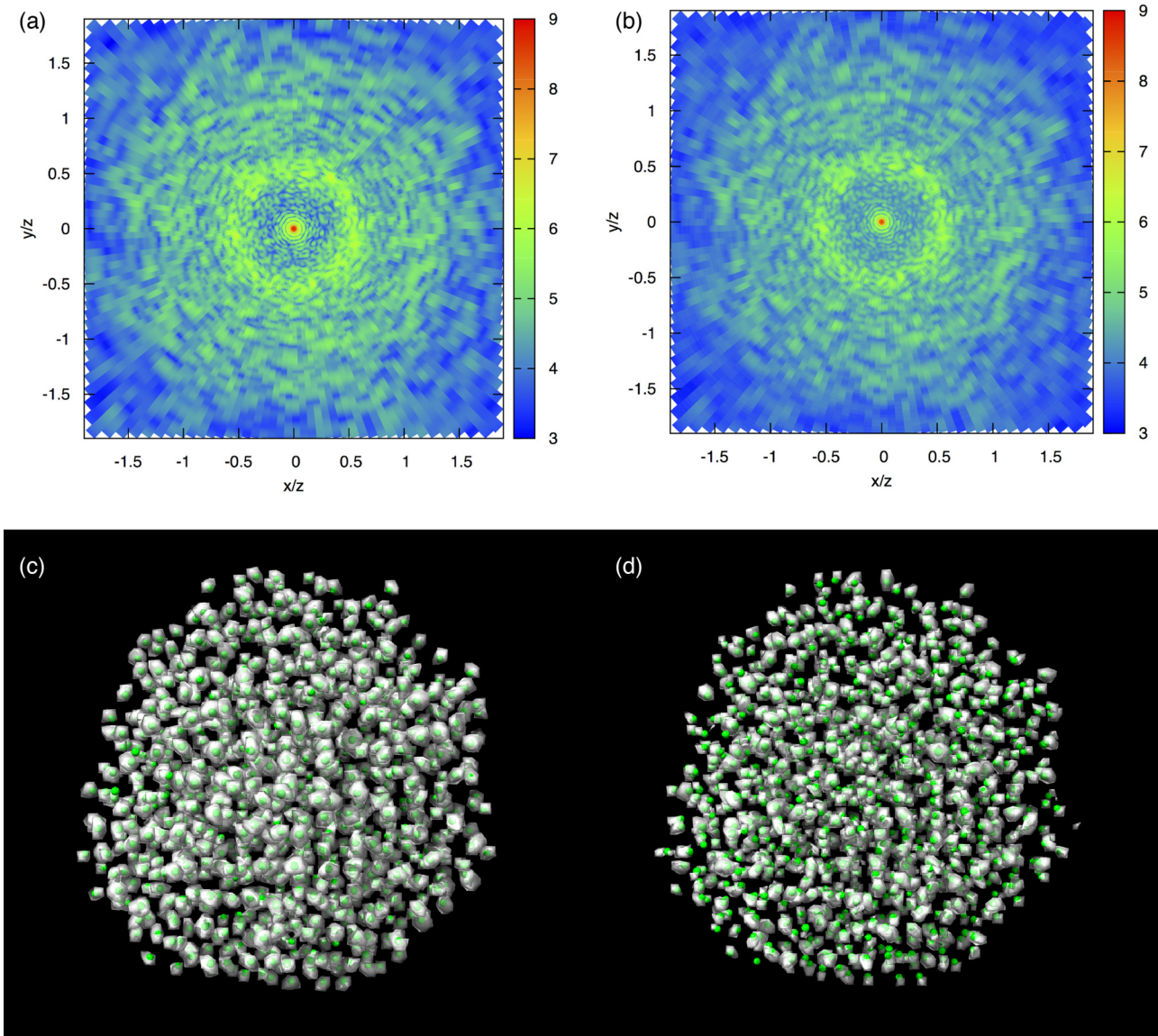
FIG. 8. Diffraction patterns of an amorphous Ar cluster calculated for a 2 fs, 8 keV pulse with a fluence of (a) 10^{12} photons/μm^2 and (b) 10^{14} photons/μm^2. The reconstructed 3D electron density calculated for a 2 fs, 8 keV pulse with a fluence of (c) 10^{12} photons/μm^2 and (d) 10^{14} photons/μm^2. The green dots show the position of atoms of an undamaged cluster and the gray surface shows the reconstruction.

with the pulse intensity) were then averaged for the duration of the x-ray pulse. While the presence of Poisson noise in the 2D scattering patterns has important consequences for the orientation process, in the 3D scattering distribution (normally an average of a great number of noisy 2D patterns) the Poisson noise is reduced and can be negligible. Therefore, Poisson noise was not included in the simulation of 3D scattering patterns.

To show that the structural information is encoded in the intensity patterns, we verified the results from RAAR method using the hybrid-input-output (HIO) phase retrieval algorithm [80]. In order to speed up the calculation, the support S needed in the HIO method is modified dynamically via the shrink-warp (SW) procedure [81]. Initially, the S is set to be the autocorrelation function of the cluster. About a total of 1000 iterations of HIO are used and the SW procedure is applied every 100 steps. At the end 100 ER iterations are used to obtain

a final electron density. The electron densities calculated from the HIO method, as shown in Fig. 7, are similar to those from the RAAR method.

APPENDIX B: 3D IMAGING OF AN AMORPHOUS CLUSTER

To show that 3D atomistic coherent x-ray diffractive imaging is not limited to systems with periodic or crystalline initial atomic arrangements, we have also examined the scattering response of an amorphous Ar cluster with 1123 atoms as a function of pulse fluence. The initial atomic positions of our amorphous cluster are obtained by first removing about 20% of the atoms from a seven-shell Ar$_{1415}$ cluster and allowing the remaining atoms to reach an equilibrium configuration. Figures 8(a) and 8(b) show the 2D patterns of the cluster with the same orientation collected from a 2 fs, 8 keV pulse with a

fluence of 10^{12} and 10^{14} photons/μm^2; the fivefold symmetry seen in Fig. 2 disappears and is replaced with a circular ring. The increased degree of electronic damage in a higher fluence (10^{14} photons/μm^2) pulse leads to reduced visibility due to both ionization and lattice motion. Using the HIO algorithm, we are able to reconstruct the 3D electron density from 3D diffraction signals ($101 \times 101 \times 101$) with a spatial resolution of 1.97 Å in each dimension. Figures 8(c) and 8(d) show that the atomistic reconstructions from a pulse with a fluence of 10^{12} and 10^{14} photons/μm^2 are similar to the undamaged structure.

APPENDIX C: EFFECTS OF ORIENTATION ON SCATTERED PHOTON NUMBERS

In order to obtain a 3D structure, scattering signals need to be collected over a range of q_x, q_y, and q_z. To do that, a set of 2D patterns corresponding to different orientations are needed as each 2D pattern gives only a limited range of q_x, q_y, and q_z [82]. This is different from the scattering of liquid or powder diffraction, where a collection of particles with random orientation is imaged, and a single 2D pattern is sufficient to give information about the pair correlation function [83]. In single-particle 3D diffractive imaging, the diffraction patterns plotted in terms
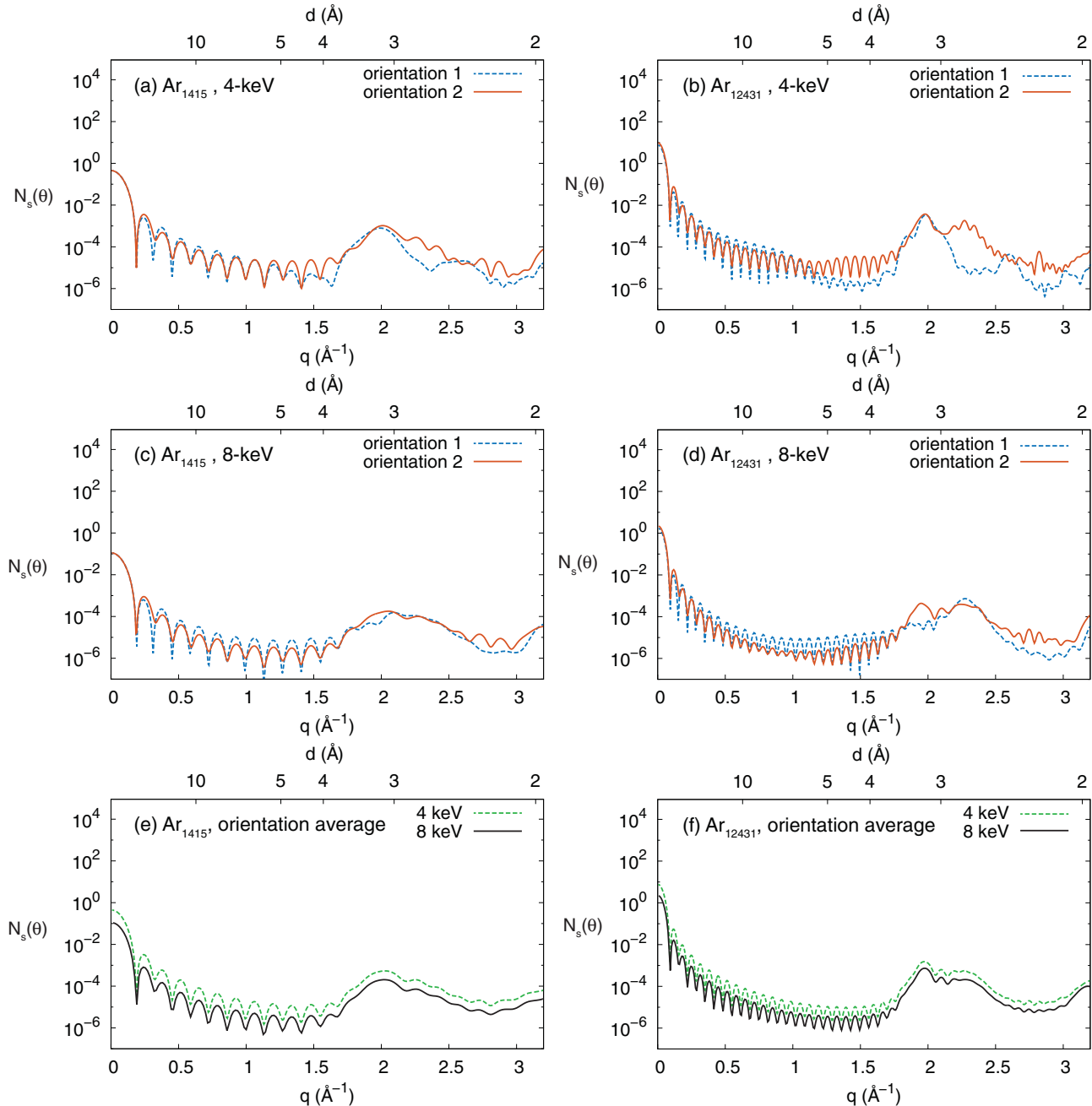

FIG. 9. Number of scattered photons per Shannon pixel (N_s) for different cluster orientations (a) Ar$_{1415}$ at 4 keV, (b) Ar$_{12431}$ at 4 keV, (c) Ar$_{1415}$ at 8 keV, and (d) Ar$_{12431}$ at 8 keV. For (a) to (d), we rotate the y axis of the cluster in orientation 1 (dashed blue lines) by 45° to obtain orientation 2 (solid red lines). N_s averaged over 100 random orientations for (e) Ar$_{1415}$ and (f) Ar$_{12431}$ at 4 keV (dashed green lines) and 8 keV (solid black lines). All cases correspond to a fluence level of 10^{11} photons/μm^2.

of scattered photons per Shannon pixel (N_s) for different orientations and photon energies can be very different from each other, as shown in panels (a)–(d) in Fig. 9. By averaging over 100 random orientations, the resulting N_s plotted as a function q for different photon energies resemble each other as expected from liquid scattering or powder diffraction.

---

[1] W. Ackermann, G. Asova, V. Ayvazyan, A. Azima, N. Baboi, J. Bähr, V. Balandin, B. Beutner, A. Brandt, A. Bolzmann *et al.*, Operation of a free-electron laser from the extreme ultraviolet to the water window, Nat. Photon. **1**, 336 (2007).

[2] P. Emma, R. Akre, J. Arthur, R. Bionta, C. Bostedt, J. Bozek, A. Brachmann, P. Bucksbaum, R. Coffee, F. J. Decker *et al.*, First lasing and operation of an ångstrom-wavelength free-electron laser, Nat. Photon. **4**, 641 (2010).

[3] T. Ishikawa, H. Aoyagi, T. Asaka, Y. Asano, N. Azumi, T. Bizen, H. Ego, K. Fukami, T. Fukui, Y. Furukawa *et al.*, A compact x-ray free-electron laser emitting in the sub-angstrom region, Nat. Photon. **6**, 540 (2012).

[4] M. Altarelli, R. Brinkmann, and M. Chergui *et al.*, Technical Design Report of the European XFEL, DESY Report No. 2006-097, 2006.

[5] C. Bostedt, S. Boutet, D. M. Fritz, Z. Huang, H. J. Lee, H. T. Lemke, A. Robert, W. F. Schlotter, J. J. Turner, and G. J. Williams, Linac coherent light source: The first five years, Rev. Mod. Phys. **88**, 015007 (2016).

[6] L. Young, E. P. Kanter, B. Krässig, Y. Li, A. M. March, S. T. Pratt, R. Santra, S. H. Southworth, N. Rohringer, L. F. DiMauro *et al.*, Femtosecond electronic response of atoms to ultra-intense x-rays, Nature (London) **466**, 56 (2010).

[7] G. Doumy, C. Roedig, S.-K. Son, C. I. Blaga, A. D. DiChiara, R. Santra, N. Berrah, C. Bostedt, J. D. Bozek, P. H. Bucksbaum *et al.*, Nonlinear Atomic Response to Intense Ultrashort X Rays, Phys. Rev. Lett. **106**, 083002 (2011).

[8] B. Rudek, S.-K. Son, L. Foucar, S. W. Epp, B. Erk, R. Hartmann, M. Adolph, R. Andritschke, A. Aquila, N. Berrah *et al.*, Ultra-efficient ionization of heavy atoms by intense x-ray free-electron laser pulses, Nat. Photon. **6**, 858 (2012).

[9] M. Hoener, L. Fang, O. Kornilov, O. Gessner, S. T. Pratt, M. Guhr, E. P. Kanter, C. Blaga, C. Bostedt, J. D. Bozek *et al.*, Ultraintense X-Ray Induced Ionization, Dissociation, and Frustrated Absorption in Molecular Nitrogen, Phys. Rev. Lett. **104**, 253002 (2010).

[10] S. Schorb, D. Rupp, M. L. Swiggers, R. N. Coffee, M. Messerschmidt, G. Williams, J. D. Bozek, S.-I. Wada, O. Kornilov, T. Möller *et al.*, Size-Dependent Ultrafast Ionization Dynamics of Nanoscale Samples in Intense Femtosecond X-Ray Free-Electron-Laser Pulses, Phys. Rev. Lett. **108**, 233401 (2012).

[11] N. Rohringer, D. Ryan, R. A. London, M. Purvis, F. Albert, J. Dunn, J. D. Bozek, C. Bostedt, A. Graf, R. Hill *et al.*, Atomic inner-shell x-ray laser at 1.46 nanometres pumped by an x-ray free-electron laser, Nature (London) **481**, 488 (2012).

[12] H. Yoneda, Y. Inubushi, K. Nagamine, Y. Michine, H. Ohashi, H. Yumoto, K. Yamauchi, H. Mimura, H. Kitamura, and T. Katayama *et al.*, Atomic inner-shell laser at 1.5-angstrom wavelength pumped by an x-ray free-electron laser, Nature (London) **524**, 446 (2015).

[13] B. Nagler, U. Zastrau, R. R. Faeustlin, S. M. Vinko, T. Whitcher, A. J. Nelson, R. Sobierajski, J. Krzywinski, J. Chalupsky, E. Abreu *et al.*, Turning solid aluminium transparent by intense soft x-ray photoionization, Nat. Phys. **5**, 693 (2009).

[14] H. Yoneda, Y. Inubushi, M. Yabashi, T. Katayama, T. Ishikawa, H. Ohashi, H. Yumoto, K. Yamauchi, H. Mimura, and H. Kitamura, Saturable absorption of intense hard x-rays in iron, Nat. Commun. **5**, 5080 (2014).

[15] D. S. Rackstraw, O. Ciricosta, S. M. Vinko, B. Barbrel, T. Burian, J. Chalupský, B. I. Cho, H.-K. Chung, G. L. Dakovski, K. Engelhorn *et al.*, Saturable Absorption of an X-Ray Free-Electron-Laser Heated Solid-Density Aluminum Plasma, Phys. Rev. Lett. **114**, 015003 (2015).

[16] E. P. Kanter, B. Krässig, Y. Li, A. M. March, P. Ho, N. Rohringer, R. Santra, S. H. Southworth, L. F. DiMauro, G. Doumy *et al.*, Unveiling and Driving Hidden Resonances with High-Fluence, High-Intensity X-Ray Pulses, Phys. Rev. Lett. **107**, 233001 (2011).

[17] C. Weninger, M. Purvis, D. Ryan, R. A. London, J. D. Bozek, C. Bostedt, A. Graf, G. Brown, J. J. Rocca, and N. Rohringer, Stimulated Electronic X-Ray Raman Scattering, Phys. Rev. Lett. **111**, 233902 (2013).

[18] M. Beye, S. Schreck, F. Sorgenfrei, C. Trabant, N. Pontius, C. Schuessler-Langeheine, W. Wurth, and A. Foehlisch, Stimulated x-ray emission for materials science, Nature (London) **501**, 191 (2013).

[19] S. Shwartz, M. Fuchs, J. B. Hastings, Y. Inubushi, T. Ishikawa, T. Katayama, D. A. Reis, T. Sato, K. Tono, M. Yabashi *et al.*, X-Ray Second Harmonic Generation, Phys. Rev. Lett. **112**, 163901 (2014).

[20] J. C. Solem, Imaging biological specimens with high-intensity soft x rays, J. Opt. Soc. Am. B **3**, 1551 (1986).

[21] R. Neutze, R. Wouts, D. van der Spoel, E. Weckert, and J. Hajdu, Potential for biomolecular imaging with femtosecond x-ray pulses, Nature (London) **406**, 752 (2000).

[22] H. N. Chapman, P. Fromme, A. Barty, T. A. White, R. A. Kirian, A. Aquila, M. S. Hunter, J. Schulz, D. P. DePonte, U. Weierstall *et al.*, Femtosecond x-ray protein nanocrystallography, Nature (London) **470**, 73 (2011).

[23] S. Boutet, L. Lomb, G. J. Williams, T. R. Barends, A. Aquila, R. B. Doak, U. Weierstall, D. P. DePonte, J. Steinbrener, R. L. Shoeman *et al.*, High-resolution protein structure determination by serial femtosecond crystallography, Science **337**, 362 (2012).

[24] T. R. Barends, L. Foucar, S. Botha, R. B. Doak, R. L. Shoeman, K. Nass, J. E. Koglin, G. J. Williams, S. Boutet, M. Messerschmidt *et al.*, De novo protein crystal structure determination from x-ray free-electron laser data, Nature (London) **505**, 244 (2014).

[25] K. Ayyer, O. M. Yefanov, D. Oberthr, S. Roy-Chowdhury, L. Galli, V. Mariani, S. Basu, J. Coe, C. E. Conrad, R. Fromme *et al.*, Macromolecular diffractive imaging using imperfect crystals, Nature (London) **530**, 202 (2016).

[26] A. Barty, C. Caleman, A. Aquila, N. Timneanu, L. Lomb, T. A. White, J. Andreasson, D. Arnlund, S. Bajt, T. R. Barends *et al.*, Self-terminating diffraction gates femtosecond

x-ray nanocrystallography measurements, Nat. Photon. **6**, 35 (2012).

[27] C. Caleman, G. Huldt, F. R. N. C. Maia, C. Ortiz, F. G. Parak, J. Hajdu, D. van der Spoel, H. N. Chapman, and N. Timneanu, On the feasibility of nanocrystal imaging using intense and ultrashort x-ray pulses, ACS Nano **5**, 139 (2011).

[28] C. Wang *et al.*, Structural basis for molecular recognition at serotonin receptors, Science **340**, 610 (2013).

[29] Q. Zhou, Y. Lai, T. Bacaj, M. Zhao, A. Y. Lyubimov, M. Uervirojnangkoorn, O. B. Zeldin, A. S. Brewster, N. K. Sauter, A. E. Cohen *et al.*, Architecture of the synaptotagmin-SNARE machinery for neuronal exocytosis, Nature (London) **525**, 62 (2015).

[30] A. Aquila, A. Barty, C. Bostedt, S. Boutet, G. Carini, D. dePonte, P. Drell, S. Doniach, K. H. Downing, T. Earnest *et al.*, The linac coherent light source single particle imaging road map, Struct. Dyn. **2**, 041701 (2015).

[31] S.-K. Son, L. Young, and R. Santra, Impact of hollow-atom formation on coherent x-ray scattering at high intensity, Phys. Rev. A **83**, 033402 (2011).

[32] H. M. Quiney and K. A. Nugent, Biomolecular imaging and electronic damage using x-ray free-electron lasers, Nat. Phys. **7**, 142 (2011).

[33] U. Lorenz, N. M. Kabachnik, E. Weckert, and I. A. Vartanyants, Impact of ultrafast electronic damage in single-particle x-ray imaging experiments, Phys. Rev. E **86**, 051911 (2012).

[34] J. M. Slowik, S.-K. Son, G. Dixit, Z. Jurek, and R. Santra, Incoherent x-ray scattering in single molecule imaging, New J. Phys. **16**, 073042 (2014).

[35] O. Y. Gorobtsov, U. Lorenz, N. M. Kabachnik, and I. A. Vartanyants, Theoretical study of electronic damage in single-particle imaging experiments at x-ray free-electron lasers for pulse durations from 0.1 to 10 fs, Phys. Rev. E **91**, 062712 (2015).

[36] S. P. Hau-Riege, R. A. London, and A. Szoke, Dynamics of biological molecules irradiated by short x-ray pulses, Phys. Rev. E **69**, 051906 (2004).

[37] B. Ziaja, A. R. de Castro, E. Weckert, and T. Möller, Modelling dynamics of samples exposed to free-electron-laser radiation with Boltzmann equations, Eur. Phys. J. D **40**, 465 (2006).

[38] U. Saalmann, and J.-M. Rost, Ionization of Clusters in Strong X-Ray Laser Pulses, Phys. Rev. Lett. **89**, 143401 (2002).

[39] Z. Jurek, G. Faigel, and M. Tegze, Dynamics in a cluster under the influence of intense femtosecond hard x-ray pulses, Eur. Phys. J. D **29**, 217 (2004).

[40] M. M. Seibert, T. Ekeberg, F. R. N. C. Maia, M. Svenda, J. Andreasson, O. Jonsson, D. Odic, B. Iwan, A. Rocker, D. Westphal *et al.*, Single mimivirus particles intercepted and imaged with an x-ray laser, Nature (London) **470**, 78 (2011).

[41] G. Huldt, A. Szöke, and J. Hajdu, Diffraction imaging of single particles and biomolecules, J. Struct. Biol. **144**, 219 (2003).

[42] T. Ekeberg, M. Svenda, C. Abergel, F. R. Maia, V. Seltzer, J.-M. Claverie, M. Hantke, O. Jonsson, C. Nettelblad, G. van der Schot *et al.*, Three-Dimensional Reconstruction of the Giant Mimivirus Particle with an X-Ray Free-Electron Laser, Phys. Rev. Lett. **114**, 098102 (2015).

[43] B. Ziaja, Z. Jurek, N. Medvedev, V. Saxena, S.-K. Son, and R. Santra, Towards realistic simulations of macromolecules irradiated under the conditions of coherent diffraction imaging with an x-ray free-electron laser, Photonics **2**, 256 (2015).

[44] G. Li, and R. Jin, Atomically precise gold nanoclusters as new model catalysts, Acc. Chem. Res. **46**, 1749 (2013).

[45] R. Jin, Atomically precise metal nanoclusters: stable sizes and optical properties, Nanoscale **7**, 1549 (2015).

[46] P.-C. Chen, X. Liu, J. L. Hedrick, Z. Xie, S. Wang, Q.-Y. Lin, M. C. Hersam, V. P. Dravid, and C. A. Mirkin, Polyelemental nanoparticle libraries, Science **352**, 1565 (2016).

[47] J. N. Clark, L. Beitra, G. Xiong, A. Higginbotham, D. M. Fritz, H. T. Lemke, D. Zhu, M. Chollet, G. J. Williams, M. Messerschmidt *et al.*, Ultrafast three-dimensional imaging of lattice dynamics in individual gold nanocrystals, Science **341**, 56 (2013).

[48] S. P. Hau-Riege, R. A. London, G. Huldt, and H. N. Chapman, Pulse requirements for x-ray diffraction imaging of single biological molecules, Phys. Rev. E **71**, 061919 (2005).

[49] G. Bortel and G. Faigel, Classification of continuous diffraction patterns: A numerical study, J. Struct. Biol. **158**, 10 (2007).

[50] G. Bortel, G. Faigel, and M. Tegze, Classification and averaging of random orientation single macromolecular diffraction patterns at atomic resolution, J. Struct. Biol. **166**, 226 (2009).

[51] N.-T. D. Loh and V. Elser, Reconstruction algorithm for single-particle diffraction imaging experiments, Phys. Rev. E **80**, 026705 (2009).

[52] R. Fung, V. Shneerson, D. K. Saldin, and A. Ourmazd, Structure from fleeting illumination of faint spinning objects in flight, Nat. Phys. **5**, 64 (2009).

[53] M. Tegze and G. Bortel, Atomic structure of a single large biomolecule from diffraction patterns of random orientations, J. Struct. Biol. **179**, 41 (2012).

[54] T. Tachibana, Z. Jurek, H. Fukuzawa, K. Motomura, K. Nagaya, S. Wada, P. Johnsson, M. Siano, S. Mondal, Y. Ito *et al.*, Nanoplasma formation by high intensity hard x rays, Sci. Rep. **5**, 10977 (2015).

[55] T. Fennel, K.-H. Meiwes-Broer, J. Tiggesbaumker, P.-G. Reinhard, P. M. Dinh, and E. Suraud, Laser-driven nonlinear cluster dynamics, Rev. Mod. Phys. **82**, 1793 (2010).

[56] G. Faigel, Z. Jurek, G. Oszlanyi, and M. Tegze, Clusters in the XFEL beam, J. Alloys Compd. **401**, 86 (2005).

[57] T. Ditmire, T. Donnelly, A. M. Rubenchik, R. W. Falcone, and M. D. Perry, Interaction of intense laser pulses with atomic clusters, Phys. Rev. A **53**, 3379 (1996).

[58] I. Last and J. Jortner, Quasiresonance ionization of large multicharged clusters in a strong laser field, Phys. Rev. A **60**, 2215 (1999).

[59] U. Saalmann and J.-M. Rost, Ionization of Clusters in Intense Laser Pulses Through Collective Electron Dynamics, Phys. Rev. Lett. **91**, 223401 (2003).

[60] C. Bostedt, H. Thomas, M. Hoener, E. Eremina, T. Fennel, K.-H. Meiwes-Broer, H. Wabnitz, M. Kuhlmann, E. Plönjes, K. Tiedtke *et al.*, Multistep Ionization of Argon Clusters in Intense Femtosecond Extreme Ultraviolet Pulses, Phys. Rev. Lett. **100**, 133401 (2008).

[61] M. Hoener, C. Bostedt, H. Thomas, L. Landt, E. Eremina, H. Wabnitz, T. Laarmann, R. Treusch, A. R. B. de Castro, and T. Möller, Charge recombination in soft x-ray laser produced nanoplasmas, J. Phys. B **41**, 181001 (2008).

[62] C. Gnodtke, U. Saalmann, and J. M. Rost, Ionization and charge migration through strong internal fields in clusters exposed to intense x-ray pulses, Phys. Rev. A **79**, 041201 (2009).

[63] T. Gorkhover, M. Adolph, D. Rupp, S. Schorb, S. W. Epp, B. Erk, L. Foucar, R. Hartmann, N. Kimmel, K. U. Kuhnel *et al.*, Nanoplasma Dynamics of Single Large Xenon Clusters Irradiated with Superintense X-Ray Pulses From the Linac Coherent Light Source Free-Electron Laser, Phys. Rev. Lett. **108**, 245005 (2012).

[64] T. Gorkhover, S. Schorb, R. Coffee, M. Adolph, L. Foucar, D. Rupp, A. Aquila, J. D. Bozek, S. W. Epp, B. Erk *et al.*, Femtosecond and nanometre visualization of structural dynamics in superheated nanoparticles, Nat. Photon. **10**, 93 (2016).

[65] C. Bostedt, E. Eremina, D. Rupp, M. Adolph, H. Thomas, M. Hoener, A. R. de Castro, J. Tiggesbaumker, K. H. Meiwes-Broer, T. Laarmann *et al.*, Ultrafast X-Ray Scattering of Xenon Nanoparticles: Imaging Transient States of Matter, Phys. Rev. Lett. **108**, 093401 (2012).

[66] K. R. Ferguson, M. Bucher, T. Gorkhover, S. Boutet, H. Fukuzawa, J. E. Koglin, Y. Kumagai, A. Lutman, A. Marinelli, and M. Messerschmidt *et al.*, Transient lattice contraction in the solid-to-plasma transition, Sci. Adv. **2**, e1500837 (2016).

[67] P. J. Ho, C. Bostedt, S. Schorb, and L. Young, Theoretical Tracking of Resonance-Enhanced Multiple Ionization Pathways in X-ray Free-Electron Laser Pulses, Phys. Rev. Lett. **113**, 253001 (2014).

[68] P. J. Ho, E. P. Kanter, and L. Young, Resonance-mediated atomic ionization dynamics induced by ultraintense x-ray pulses, Phys. Rev. A **92**, 063430 (2015).

[69] J. H. Hubbell, W. J. Veigele, E. A. Briggs, R. T. Brown, D. T. Cromer, and R. J. Howerton, Atomic form factors, incoherent scattering functions, and photon scattering cross sections, J. Phys. Chem. Ref. Data **4**, 471 (1975).

[70] J. Chihara, Difference in x-ray scattering between metallic and non-metallic liquids due to conduction electrons, J. Phys. F **17**, 295 (1987).

[71] B. Crowley, and G. Gregori, Quantum theory of Thomson scattering, High Energ. Dens. Phys. **13**, 55 (2014).

[72] O. Klein, and Y. Nishina, Über die Streuung von Strahlung durch freie Elektronen nach der neuen relativistischen Quantendynamik von Dirac, Z. Phys. **52**, 853 (1929).

[73] B. F. Murphy, T. Osipov, Z. Jurek, L. Fang, S. K. Son, M. Mucke, J. H. D. Eland, V. Zhaunerchyk, R. Feifel, L. Avaldi *et al.*, Femtosecond x-ray-induced explosion of C_{60} at extreme intensity, Nat. Commun. **5**, 4281 (2014).

[74] C. H. Yoon, M. V. Yurkov, E. A. Schneidmiller, L. Samoylova, A. Buzmakov, Z. Jurek, B. Ziaja, R. Santra, N. D. Loh, T. Tschentscher *et al.*, A comprehensive simulation framework for imaging single particles and biomolecules at the European X-ray Free-Electron Laser, Sci. Rep. **6**, 24791 (2016).

[75] O. Ciricosta, S. M. Vinko, H.-K. Chung, B.-I. Cho, C. R. Brown, T. Burian, J. Chalupsky, K. Engelhorn, R. W. Falcone, C. Graves *et al.*, Direct Measurements of the Ionization Potential Depression in a Dense Plasma, Phys. Rev. Lett. **109**, 065002 (2012).

[76] S.-K. Son, R. Thiele, Z. Jurek, B. Ziaja, and R. Santra, Quantum-Mechanical Calculation of Ionization-Potential Lowering in Dense Plasmas, Phys. Rev. X **4**, 031004 (2014).

[77] P. J. Ho and C. Knight (unpublished).

[78] S. P. Hau-Riege, S. Boutet, A. Barty, S. Bajt, M. J. Bogan, M. Frank, J. Andreasson, B. Iwan, M. M. Seibert, J. Hajdu *et al.*, Sacrificial Tamper Slows Down Sample Explosion in FLASH Diffraction Experiments, Phys. Rev. Lett. **104**, 064801 (2010).

[79] D. R. Luke, Relaxed averaged alternating reflections for diffraction imaging, Inverse Probl. **21**, 37 (2004).

[80] J. R. Fienup, Phase retrieval algorithms: a comparison, Appl. Opt. **21**, 2758 (1982).

[81] S. Marchesini, H. He, H. N. Chapman, S. P. Hau-Riege, A. Noy, M. R. Howells, U. Weierstall, and J. C. H. Spence, X-ray image reconstruction from a diffraction pattern alone, Phys. Rev. B **68**, 140101 (2003).

[82] P. J. Ho, D. Starodub, D. K. Saldin, V. L. Shneerson, A. Ourmazd, and R. Santra, Molecular structure determination from x-ray scattering patterns of laser-aligned symmetric-top molecules, J. Chem. Phys. **131**, 131101 (2009).

[83] J. Als-Nielsen and D. McMorrow, *Elements of Modern X-ray Physics* (John Wiley & Sons, Inc., New York, 2011), pp. 113–146.